Energy & Environmental Science

ROYAL SOCIETY OF CHEMISTRY

PAPER

Published on 14 October 2026
Licensed under CC-BY 4.0

Check for updates

Cite this: DOI: 10.1039/d6ee03199d

Cross-interface diffusion-driven exsolution of praseodymium oxide nanoparticles for enabling electrolysis at industrially relevant temperatures in protonic ceramic cells

Nannan Li,[a] Leila Zouridi,[b] Vassilios Binas,[b] Wisse M. Hersbach,[c] Penghui Hou,[d] Shaoqi Zhan,*[e] Hendrik H. van de Bovenkamp,[a] Aayan Banerjee,[c] John T. S. Irvine[f] and Vasileios Kyriakou*[a]

Received 17th May 2026,
Accepted 5th October 2026

DOI: 10.1039/d6ee03199d

rsc.li/ees

Protonic ceramic electrolysis cells (PCECs) can unlock direct electrification of catalytic processes towards intensification and operation at intermediate temperatures (400–650 °C). A primary challenge, however, is the development of a steam splitting electrocatalyst (positrode) that will enable hydrogen production. Here, we have developed highly efficient and self-configured positrodes, consisting of a triple-conducting (H^+, O^{2-}, e^-) $Pr_{0.95}Ca_{0.05}Ni_{0.5}Co_{0.5}O_{3-\delta}$ perovskite matrix and exsolved praseodymium oxide nanoparticles. We show for the first time that nanoparticle nucleation is triggered by cross electrode–electrolyte interface ion diffusion by simply sintering in ambient air. To boost nanoparticles' population, we also employ strategies such as acid treatment to control surface defects. This approach doubles the electrochemical performance compared to the pristine cell, accompanied by >95% faradaic efficiency and exceptional durability for >500 h. Our work exemplifies how the previously unexplored interfacial ion interactions can be engineered to enable highly efficient renewable hydrogen production at industrially relevant temperatures.

Broader context

Electrochemical conversion technologies hold significant potential for advancing Power-to-X (X: chemical or fuel) platform towards renewable energy storage. Among them, protonic ceramic electrolysis cells (PCECs) are particularly appealing due to their operation in the industrially attractive intermediate temperature range which may enable direct electrification and intensification of critical (de)hydrogenation processes. However, to achieve efficient and stable operation in PCECs, electrocatalysts are required to accelerate proton generation from steam electrolysis. Herein, we report on self-configured electrocatalysts consisting of triple conducting oxides and exsolved praseodymium oxide nanoparticles of exceptional catalytic properties. We identify that the previously unaddressed but critical interactions of the ceramic electrolyte and the electrode at the ion level are responsible for triggering the exsolution of the anchored nanoparticles. Besides the elucidation of this unique cross-interfacial interaction, we exemplify how to exploit this phenomenon for doubling the electrochemical performance for green hydrogen production at intermediate temperatures compared to the pristine cells while maintaining >500 h of stable operation.

[a] Engineering and Technology Institute Groningen (ENTEG), University of Groningen, Nijenborgh 3, Groningen, 9747 AG, The Netherlands. E-mail: v.kyriakou@rug.nl
[b] Institute of Electronic Structure and Laser, Foundation for Research and Technology-Hellas, Heraklion 70013, Greece
[c] Sustainable Electrochemical Engineering and Digitalisation (SEED), Department of Chemical Engineering, University of Twente, PO Box 217, Enschede, 7500 AE, The Netherlands
[d] Device Physics of Complex Materials, Zernike Institute for Advanced Materials, University of Groningen, Nijenborgh 3, Groningen, 9747 AG, The Netherlands
[e] Department of Chemistry – Ångström, Molecular Biomimetics, Uppsala University, Box 523, 751 20 Uppsala, Sweden. E-mail: shaoqi.zhan@kemi.uu.se
[f] School of Chemistry, University of St Andrews, St Andrews, Scotland, KY16 9ST, UK

Introduction

Protonic ceramic cells are unique electrochemical devices with the ability to operate as both flexible fuel cells and electrolysers.[1,2] While these features are shared with their solid oxide counterparts, the lower activation energy for proton conduction (0.4–0.6 eV) compared to that of the oxide ion (>0.8 eV) can allow operation at intermediate temperatures (400–650 °C).[3,4] Unlocking the intermediate temperature range could be a game-changer for ceramic cells since the established efficiency will be combined with inexpensive stainless steel-based interconnects and faster device start-up

procedures.[5] In addition, enabling electrochemistry at such industrially-relevant temperatures would bridge them with established chemical processes towards exploiting waste heat or even enabling direct electrosynthesis of chemical fuels (hydrocarbons, ammonia, and methanol) beyond hydrogen.[6–8]

One of the prerequisites for such applications is to deliver high proton flux, either when targeting hydrogen production from electrolysis or its *in situ* production (as protons) and conversion to chemical fuels. In PCECs, steam is converted to oxygen and protons (eqn (1)) at the positrode, with the latter to be transported to the negatrode through the electrolyte:[9]

$$H_2O(g) + O_O^{\times} + V_O^{\bullet\bullet} \leftrightarrows 2OH_O^{\bullet} \quad (1)$$

Protonic ceramics, however, such as the state-of-the-art $BaZrO_3$–$BaCeO_3$ mixed oxides, are not exclusively proton-conducting materials.[10,11] Perovskite oxides exhibit mixed ion (protons and oxygen ion) and electron conductivity and their transference number ratios are determined by temperature, gas atmosphere, electrolyte chemical composition and cell polarization.[12] In the case of steam electrolysis, the situation becomes more complex due to the competitive absorption between water vapor and oxygen towards incorporation into the oxygen vacancies. While the hydration reaction produces the desired charge defect and protons are transferred through the membrane (eqn (1)), molecular oxygen incorporation into the oxygen vacancy creates electron holes *via* a side oxidation reaction (eqn (2)), thus resulting in p-type electronic leakage and low faradaic efficiency:[10]

$$\frac{1}{2}O_2(g) + V_O^{\bullet\bullet} \leftrightarrows 2h^{\bullet} + O_O^{\times} \quad (2)$$

Hence, efficient and stable electrocatalysts for accelerating the oxygen evolution reaction (OER) at intermediate temperatures (<650 °C) are critical. Since the reaction mechanism involves several steps along with oxygen and electron participation besides hydration, triple conducting (H^+, O^{2-}, e^-) oxides (TCO) can extend the electrocatalytically active sites. Since the first demonstration by O'Hayre's group with a $BaCo_{0.4}Fe_{0.4}Zr_{0.1}Y_{0.1}O_{3-\delta}$[13] perovskite, several other chemistries have shown similar properties with $PrNi_{0.5}Co_{0.5}O_{3-\delta}$ (PNC),[14] $Ba_{1-x}Gd_{0.8}La_{0.2+x}Co_2O_{6-\delta}$,[15] $PrBa_{0.5}Sr_{0.5}Co_{0.5}Fe_{0.5}O_{6-\delta}$ and $Gd_{0.3}Ca_{2.7}Co_{3.82}$ $Cu_{0.18}O_{9-\delta}$,[16–18] to exhibit promising results. Nonetheless, the gap between commercialization and experimentation still exists for intermediate temperature applications in terms of stability or chemical complexity.[19,20]

Different strategies have been utilised to increase electrical efficiencies through the manipulation of the intrinsic properties of the positrode. Among these, rational doping and nanostructuring through infiltration or redox exsolution have been proven highly effective in altering oxygen vacancy concentration and enhancing water uptake.[21–27] For instance, K^+ doping at the A-site of $BaCo_{0.4}Fe_{0.4}Zr_{0.18}Y_{0.02}O_{3-\delta}$ (BCFZY) resulted in both lower formation energy of bulk oxygen vacancies and stimulation of BaO precipitation in wet atmospheres with considerable electrocatalytic properties.[21] Similarly, Chen *et al.* enhanced the properties of $Pr_2Ni_{0.6}Co_{0.4}O_{4-\delta}$ through its self-configuration into a dual phase of $Pr_4Ni_{1.8}Co_{1.2}O_{10-\delta}$ and Pr_6O_{11} phases.[25]

Inspired by these findings, here we have created a self-configured positrode consisting of a triple-conducting PNC-based perovskite host and highly dispersed exsolved Pr_6O_{11} nanoparticles of 10 nm by annealing the cell assembly in ambient air. By exploring different ceramic electrolytes, we prove the strong correlation of the amount of exsolved atoms with the Ce doping of the electrolyte which resulted in the precipitation of catalytically active nanoparticles. We further utilized rational doping of Ca at the A-site and acid treatment to increase the defect concentration and provide preferential nucleation sites for exsolution to boost the nanoparticles' population. Our extensive characterization studies revealed that the combined exsolution and Ca doping boosted oxygen surface exchange kinetics and water uptake, leading to exceptional electrocatalytic behaviour by doubling the unmodified PNC hydrogen production at the thermoneutral voltage, accompanied by up to 95% faradaic efficiency and exceptional stability for >500 h. Our results highlight a previously unaddressed effect of the ceramic electrolyte through ion exchange at the interface that can be essential for unlocking highly efficient H_2O electrolysis at industrially relevant temperatures.

Results

Crystal structure and morphology of the electrocatalysts

Four types of samples were synthesized using the wet-method (Methods, SI), namely bare $PrNi_{0.5}Co_{0.5}O_{3-\delta}$ (PNC), Ca-doped $Pr_{0.95}Ca_{0.05}Ni_{0.5}Co_{0.5}O_{3-\delta}$ (PCNC), acid-treated PNC (PNC-AT), and acid-treated PCNC (PCNC-AT). Following calcination, the crystallographic properties were evaluated by X-ray diffraction (XRD) and Rietveld refinement (Fig. 1a–c). Fig. 1a and Table S1 show that the PNC and PCNC have an orthorhombic perovskite structure (space group: *Pbnm*) with a minor NiO secondary phase, whereas CaO appears as a secondary phase in the Ca-doped sample. Compared to PNC (a = 5.405 Å, b = 5.380, c = 7.622 Å, V = 221.622 Å^3), no obvious lattice expansion is detected in the PCNC sample (a = 5.4043 Å, b = 5.387 Å, c = 7.620 Å, V = 221.858 Å^3) due to the similar ionic radii of Ca^{2+} (1.18 Å) to Pr^{3+} (1.179 Å) when occupying A-sites in the perovskite structure. PNC and PCNC powders were treated with acetic acid to remove CaO.[28,29] The treatment preferentially removed CaO but resulted in a slight increase in the NiO secondary phase during the process (Fig. 1b and Table S1). This result was also supported by the XPS analysis in which the originally well above nominal Ca concentration in PCNC significantly decreased from 5.8 to 2.0% after acid treatment (Fig. 1d) and the inductively coupled plasma-optical emission spectrometry (ICP-OES) in which the Ca amount was decreased by almost 2% (Fig. S2a–d), confirming that acetic acid selectively etched the CaO secondary phase that was not incorporated into the crystal structure. The slightly decreased lattice parameters and unit cell volume on PNC and PCNC after acetic

 This journal is © The Royal Society of Chemistry 2026

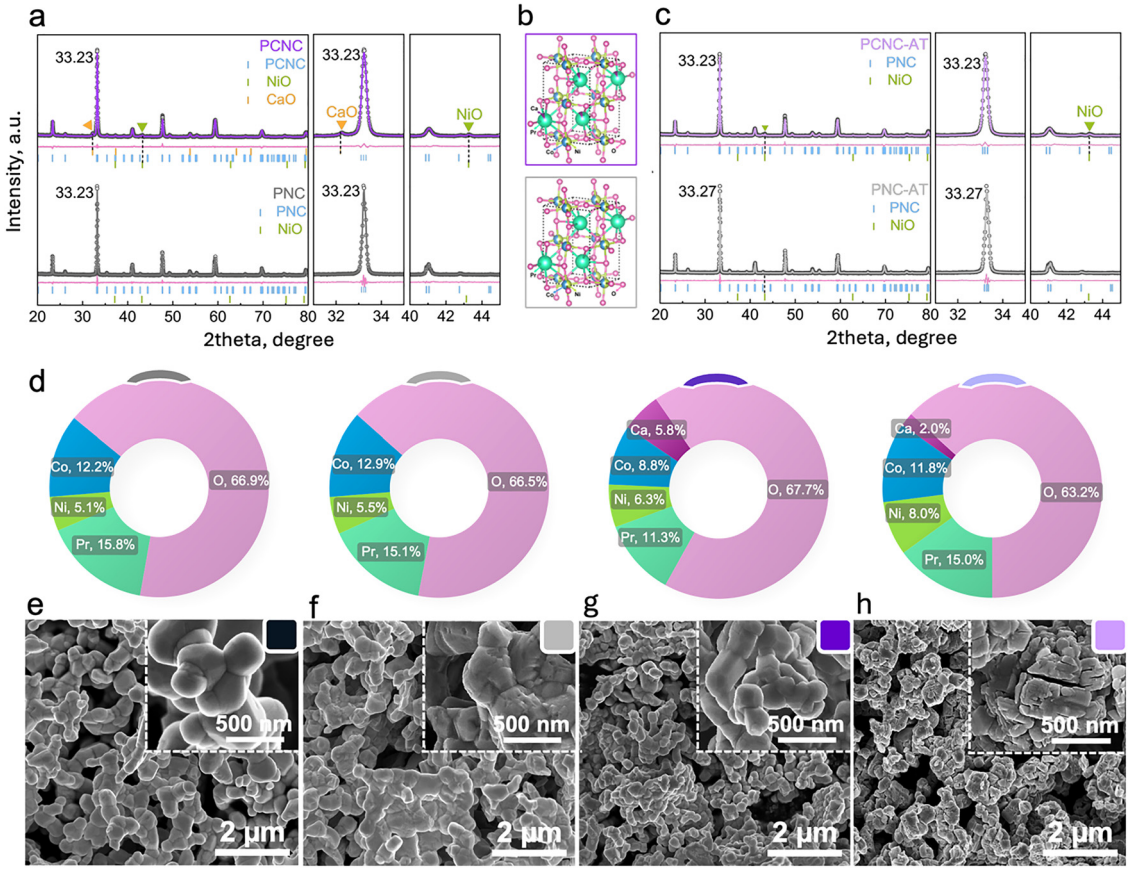


Fig. 1 Characterisation studies of the as-prepared positrodes. Crystal structure, morphology, and microstructure of the samples following wet synthesis and calcination at 1000 °C for 5 h. (a) XRD patterns and the corresponding Rietveld refinement revealing the existence of CaO (PCNC) and NiO phases. (b) Crystal lattice of PNC and PCNC. (c) XRD patterns following acid treatment where the CaO peak disappears for the PCNC-AT sample. (d) Surface quantification pie charts as calculated by the XPS survey revealing Ca segregation before acid treatment. The corresponding SEM images displaying the surface of (e) PNC, (f) PNC-AT, (g) PCNC and (h) PCNC-AT powders.

acid treatment are likely attributable to the increased Ni segregation from the bulk.

The morphological characteristics were investigated by scanning electron microscopy (SEM). As displayed in Fig. 1e–h, the etched samples exhibit a rougher surface following acid treatment implying a higher defect concentration. EDX analysis shown in Fig. S1 reveals a relatively uniform distribution of all elements but with Ca and Ni segregation in PCNC, in agreement with the XRD results. In addition, BET analysis revealed that the acid treatment led to a 2–3 times increase in surface area (Fig. S2e and f).

Evaluation of key properties for oxygen evolution electrocatalysis

Chemical stability and structural stability under the reaction-relevant conditions (gas atmosphere, temperature) are essential for the electrode applicability in PCECs. Hence, we performed *in situ* high-temperature XRD analysis of the etched samples at temperatures between 30 and 650 °C in 10% H_2O/air and dry air. The XRD patterns and lattice parameters (Fig. 2a, b and Fig. S3, Tables S2–S5) revealed that during exposure of the samples to reaction conditions, no phase decomposition or new phase formation was observed besides the peak shift due to thermal expansion, indicating adequate thermal and chemical stability. The lattice parameters for the different temperatures and conditions are summarized in Tables S2–S5. Furthermore, the thermal expansion coefficients (TECs) derived from lattice parameter (*a*, *b*, *c*) change were calculated, shown in Fig. S4–S6. Notably, exposure to 10% H_2O–air increases the TEC of PCNC-AT to $\sim 17.3 \times 10^{-6}$ K^{-1} from $\sim 16.0 \times 10^{-6}$ K^{-1} in dry air, whereas the PNC-AT exhibits negligible variation (dry air: 15.8×10^{-6} K^{-1}, 10% H_2O–air: 15.5×10^{-6} K^{-1}). The higher TEC of PCNC-AT in wet air indicates a more pronounced lattice response to hydration, suggesting that Ca doping promotes the water uptake capacity of the PNC materials.

The bulk electrical conductivity of the acid-treated samples was also evaluated by employing the four-probe method under dry and wet air conditions (10% H_2O) as a function of temperature (400–650 °C). As illustrated in Fig. S7, the conductivity of PNC-AT and PCNC-AT increased with temperature, demonstrating the typical p-type semiconductor behaviour under oxidizing conditions. Ca doping increased the conductivity reaching values between 114 and 187 S cm^{-1} in wet air, at 400 and 650 °C, respectively, compared to 106 and 185 S cm^{-1}

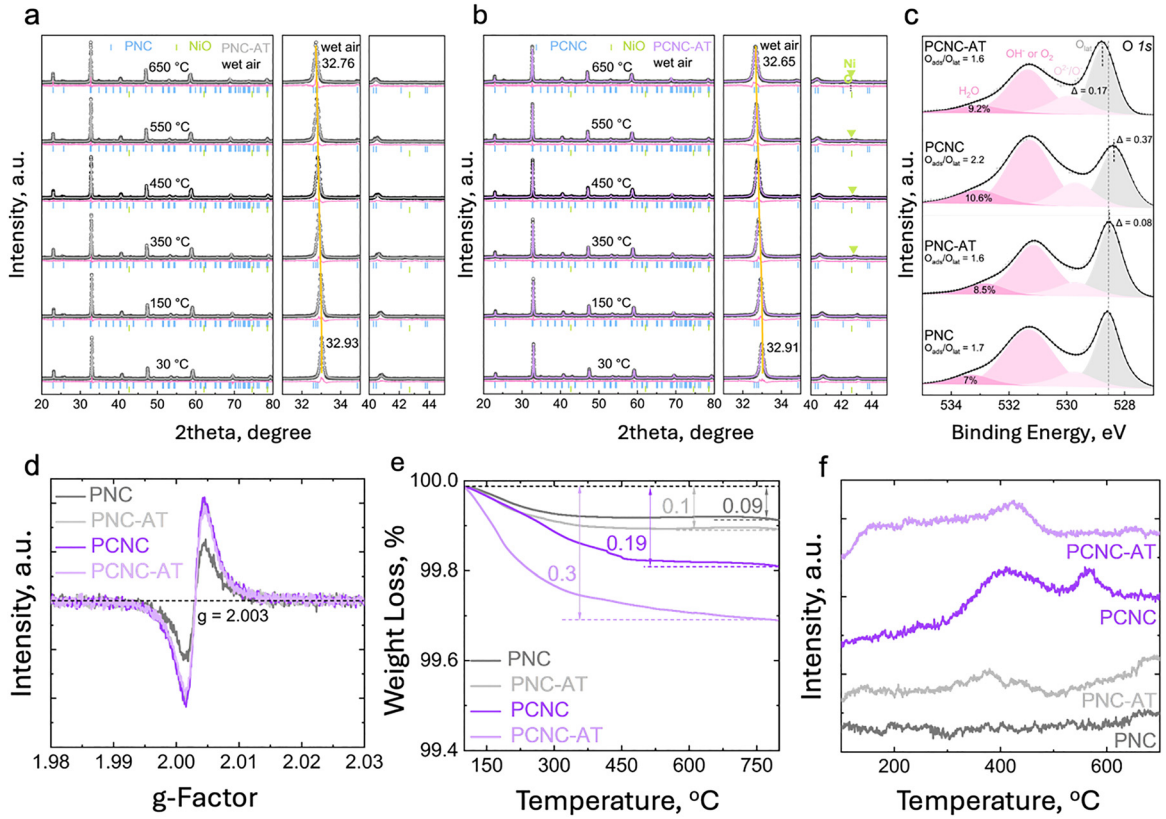


Fig. 2 Evaluation of critical properties for OER performance in PCECs. High temperature *in situ* XRD patterns of (a) PNC-AT and, (b) PCNC-AT samples in 10%H_2O/air. Evaluation of oxygen chemistry and exchange kinetics. (c) XPS spectra of O 1s to distinguish oxygen species at the surface of the calcined samples. (d) EPR for the identification of the bulk oxygen vacancy concentration. (e) TGA in air and (f) O_2-TPD profiles in the temperature range of 100–700 °C for evaluating oxygen surface exchange kinetics.

for PNC-AT in the same temperature range. The conductivity of PNC-AT dropped on switching from dry to wet air above 500 °C whereas PCNC-AT remained stable which could indicate better phase stability in the presence of Ca.

X-ray photoelectron spectroscopy (XPS) was carried out to investigate modifications in the valence state of ions. Fig. S8 illustrates the Co 2p and Ni 2p spectra, whereby both cations exhibit mixed oxidation states.[21] The average valence of the Co ions was slightly lower in the Ca-free samples, while no clear difference was observed for Ni. Most likely, Pr^{3+}substitution by Ca^{2+} increases the B-site valence state to balance charge neutrality and may explain the higher electrical conductivity of the PCNC-AT sample. Oxygen chemistry and vacancies at the surface are critical for high-performance positrodes, thus O 1s was also analyzed.[14,18,30,31] Fig. 2c spectra can be deconvoluted to four peaks, namely lattice oxygen (≈528.6 eV, O_{lat}) bonded to metal ions, highly oxidative oxygen species (≈529 eV, O_2^{2-}/O^-), chemisorbed oxygen species (≈531.5 eV, OH^-/O_2), and surface-adsorbed water (533 eV, H_2O).[32,33] The O_{lat} peak position decreases by 0.37 eV due to Ca doping due to the weakened bond strength between the metal ion and O_{lat} due to the electropositive Ca doping over Pr and/or the presence of more defects.[34] Among the samples, PCNC exhibited the highest value of an O_{ads}/O_{lat} ratio of 2.2 (where O_{ads}: O_2^{2-}/O^- and OH^-/O_2), implying a stronger capacity of PCNC for water uptake/proton diffusion and oxygen exchange at the surface than PNC.[35,36]

Both bulk and surface oxygen vacancies participate in the involved electrochemical reactions, and thus their concentration is critical for the OER.[37] Here, electron paramagnetic resonance (EPR) was employed to detect electron pairs in oxygen vacancies (Fig. 2d). The signal intensity followed the order PCNC-AT > PCNC > PNC-AT > PNC, confirming that Ca doping and acid treatment increased the concentration of oxygen vacancies. This result is corroborated by the TGA profiles in air (Fig. 2e) for the relative mass loss. In addition, we performed temperature-programmed desorption of oxygen (O_2-TPD) to investigate the nature of oxygen species. The peaks below 550 °C are attributed to the desorption of chemisorbed oxygen from surface oxygen vacancies, whereas above 550 °C, desorption of lattice oxygen is expected.[38] As depicted in Fig. 2f, the PCNC exhibits the largest peak area, implying an important role of Ca presence in accelerating oxygen exchange kinetics.[39,40]

Exsolution of socketed praseodymium oxide nanoparticles

The as-prepared positrode powders were deposited on $BaCe_{0.7}Zr_{0.1}Y_{0.1}Yb_{0.1}O_{3-\delta}$ (BZCYYb1711)/NiO-BZCYYb1711 half-cells and sintered at 900 °C for 2 h (Fig. 3a). Protonic ceramics with high Ce content, although less chemically stable, were selected due to the high faradaic efficiencies reported.[41]

 This journal is © The Royal Society of Chemistry 2026

Following sintering, the electrodes were examined by transmission electron microscopy (TEM) and SEM, revealing the emergence of nanoparticles at the surface of all positrodes (Fig. 3b–j). High-resolution TEM (HR-TEM) images revealed the characteristic *d*-spacings for (111) and (200) planes of Pr_6O_{11} (PDF#42-1121, PDF#89-0573) (Fig. 3b, c and Fig. S9). The high-angle annular dark-field (HAADF) in Fig. 3d, e and Fig. S10 and the corresponding EDX elemental mapping (Fig. 3f and Fig. S11) confirmed that the nanoparticles are rich in Pr and O with almost negligible content of other elements.

Due to the small size of the nanoparticles, a direct XRD analysis on the electrodes was not adequate for identifying the characteristic peaks for Pr_6O_{11} (or closely related PrO_x species). Hence, we prepared powder samples of positrode and electrolyte mixtures at different ratios (positrode/electrolyte: 50/50, 75/25, 90/10, 100/0). The mixtures were sintered at 1000 °C for 2 h as in the case of electrode sintering for enabling possible interactions between the ceramic electrolyte and the positrode powders. SEM analysis of Fig. S12 and S13 depicts the emergence of nanoparticles from PCNC-AT powder only after its calcination in the presence of the BZCYYb electrolyte, supporting our electrode evidence. The nanoparticles in the present case had different characteristics from the electrode case in Fig. 3, exhibiting larger size (20–30 nm) and lower population. The XRD analysis of all mixed powders, however, revealed the characteristic reflections of (111) PrO_x at 28.5–28.6° which can be explained either by the completion of oxidation to PrO_2 or by a slight shift in Pr_6O_{11} with the latter matching the characteristic 0.315 nm *d*-spacing from the HAADF-STEM analysis (Fig. S15). Lastly, we also repeated the O_2-TPD in order to evaluate possible modifications of the oxygen adsorption/desorption capacity of the positrodes due to the interaction with the BZCYYb1711 electrolyte and the exsolution effects. Fig. S15 shows that while the trend between the PNC-based materials is the same, the oxygen exchange capacity has been boosted, implying a key role of the electrolyte and the population of PrO_x exsolved species.

SEM analysis was employed to investigate the population and size distribution of nanoparticles exsolving on the different electrodes deposited on BZCYYb1711 after sintering at 900 °C.

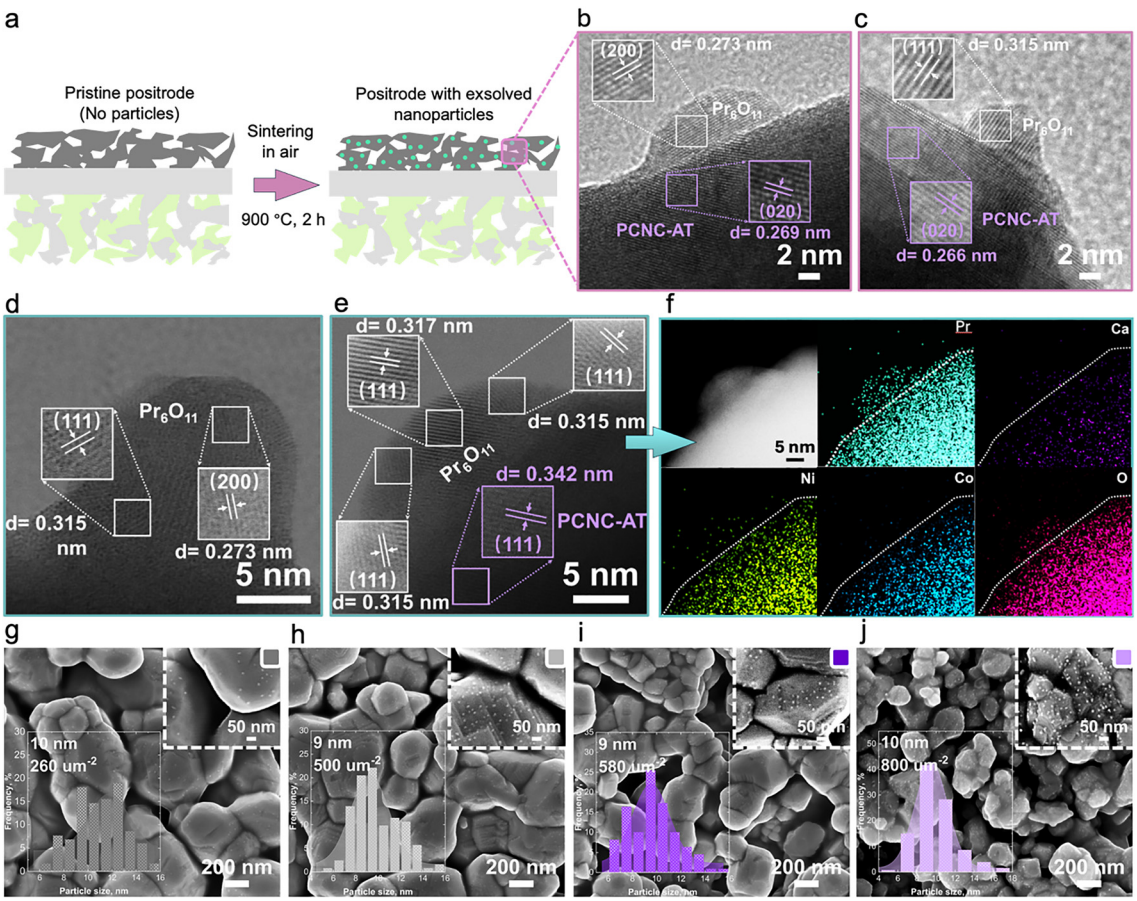


Fig. 3 Characterization of the exsolved nanoparticles following electrode and electrolyte sintering. (a) Schematic illustration of the electrode decorating process with exsolved nanoparticles by sintering in air at 900 °C. (b) and (c) High-resolution TEM images and (d) and (e) HAADF images of the PCNC-AT electrode at different areas. (f) HAADF-STEM image with the corresponding elemental mapping for the PCNC-AT electrode which exhibited the highest population of exsolved particles. SEM images of (g) PNC, (h) PNC-AT, (i) PCNC and (j) PCNC-AT positrodes deposited on BZCYYb1711 ceramic electrolyte and sintering at 900 °C for 2 h in ambient air (inset: average diameter and population density of exsolved nanoparticles, top right inset: magnified SEM images).

Uniformly dispersed particles with a population density of ~260 particles μm^{-2} were observed on the PNC (Fig. 3g) while the acid washing and Ca doping doubled the particle population to ~500 and ~580 μm^{-2} for PNC-AT and PCNC, respectively (Fig. 3h–i). The sample with the highest population was PCNC-AT with a population of ~800 μm^{-2} (Fig. 3j). The observed population order follows the same trend as the oxygen vacancy concentration intensity in EPR (Fig. 2d). The exsolution process is known to be facilitated by lattice defects, such as oxygen vacancies that act as nucleation sites for the precipitating species.[42] Here, the doping of Ca in combination with acid treatment enhanced the concentration of oxygen vacancies and point defects (higher surface roughness), thereby decreasing the free energy of Pr precipitation.

To elucidate the phenomenon, we investigated parameters that could affect exsolution, namely sintering temperature and ceramic electrolyte material (substrate). For our analysis, we employed the PCNC-AT sample with the highest nanoparticle population. First, we increased the sintering temperature to 1000 °C by keeping the ramp rate (2 °C min^{-1}) and duration at the peak temperature (2 h) constant. Fig. 4a displays a small increase in population to 950 from 800 μm^{-2} and in the average size (to ~13 from ~10 nm) compared to those of the sample sintered at 900 °C.

Subsequently, we explored whether the ceramic electrolyte chemistry could influence exsolution properties. PCNC-AT was therefore deposited on ceramic electrolytes of different chemistries and sintered at 1000 °C for 2 h. As can be seen in Fig. 4b–e and Fig. S16a, the population gradually decreases by lowering

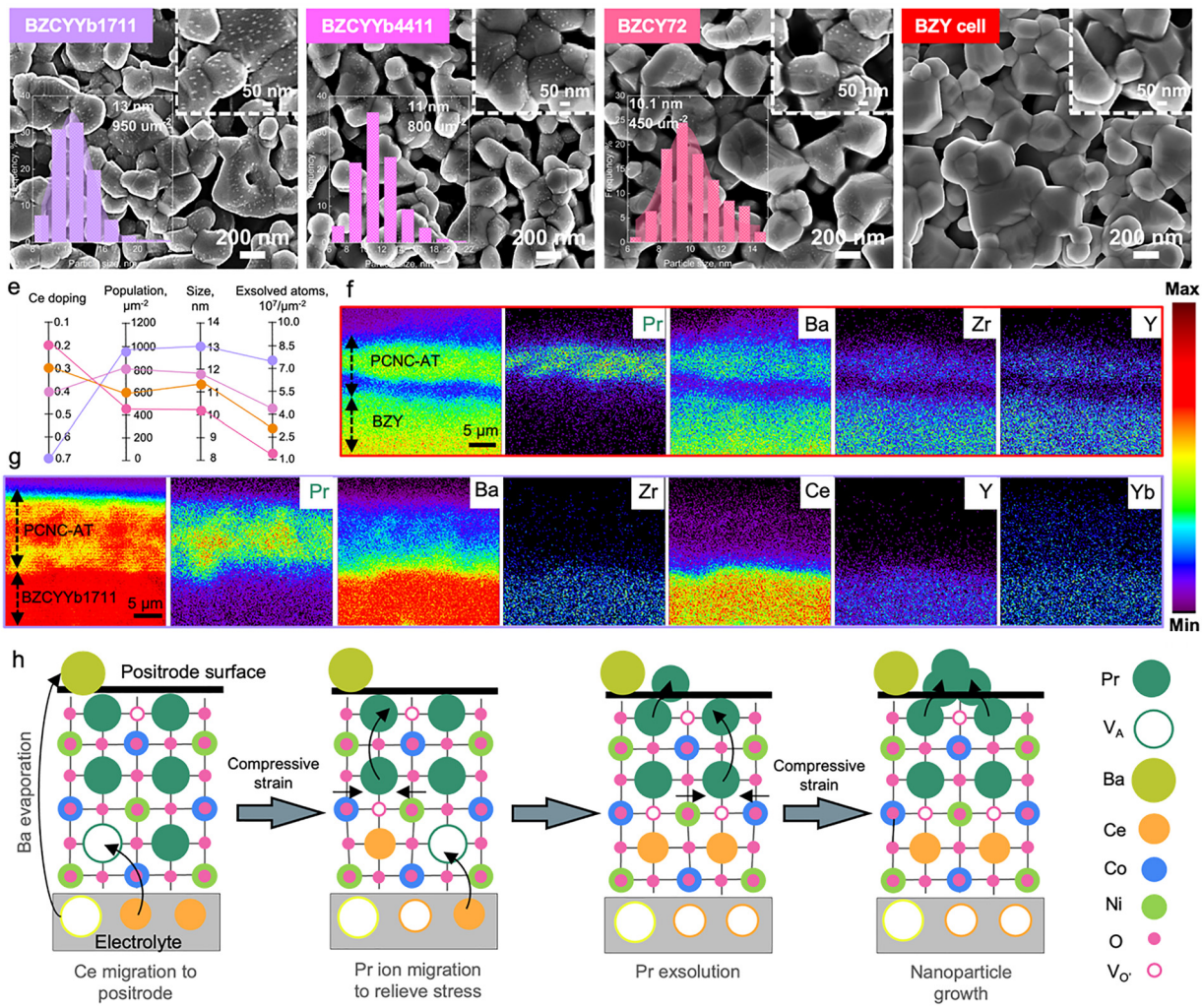


Fig. 4 Effect of the ceramic electrolyte on the exsolved Pr_6O_{11} nanoparticles. SEM images of the PCNC-AT electrode deposited and sintered with the ceramic electrolyte at 1000 °C for 2 h: (a) BZCYYb1711, (b) BZCYYb4411, (c) BZCY72 and (d) BZY. (e) Analysis of the nanoparticle characteristics for the different ceramic electrolytes. The case of BZCYYb5311 is shown in Fig. S16a. TOF-SIMS analysis of PCNC-AT/BZY (f) and PCNC-AT/BZCYYb1711 (g) interfaces which reveals Ba presence in both electrolytes, as well as possible Ce and Yb migration from the BZCYYb1711 electrolyte at the PCNC-AT positrode. (h) Possible mechanism for the PrO_x exsolution mechanism. Ba is evaporated from all ceramic electrolyte substrates; however, in the case of Ce-containing electrolytes, this process releases cerium oxides that interact at the interface, resulting in exsolution of PrO_x nanoparticles due to compressive lattice strain and oxygen vacancies.

 This journal is © The Royal Society of Chemistry 2026

the Ce content in the electrolyte, with ~800 μm^{-2} on $BaZr_{0.4}Ce_{0.4}Y_{0.1}Yb_{0.1}O_{3-\delta}$ (BZCYYb4411, Fig. 4b), ~600 μm^{-2} on $BaZr_{0.5}Ce_{0.3}Y_{0.1}Yb_{0.1}O_{3-\delta}$ (BZCYYb5311, Fig. S16a) and ~450 μm^{-2} on $BaZr_{0.7}Ce_{0.2}Y_{0.1}O_{3-\delta}$ (BZCY72, Fig. 4c). It should be pointed out however that the latter composition did not contain Yb. When a Ce-free electrolyte was employed, *i.e.*, $BaZr_{0.9}Y_{0.1}O_{3-\delta}$ (BZY, Fig. 4d) and other known protonic ceramics, such as La_6WO_{12} (LWO, Fig. S16b), no nanoparticles were observed. For consistency, we also re-sintered PCNC-AT fresh positrode powder at 1000 °C for 2 h, in which no precipitation was detected as well (Fig. S16c).

By observing the relationship between Ce doping and the exsolution process, we tried to quantify a possible relationship between them. Assuming Pr_6O_{11} (most probable phase based on *d*-spacing from HAADF-STEM and XRD) spherical particles and for known density, we can estimate the total number of exsolved atoms which can be plotted against the corresponding Ce doping of the electrolyte to identify possible correlation. Fig. S17 reveals that the number of exsolved atoms increases with Ce amount, exhibiting an almost linear relationship, implying its strong effect on Pr ion precipitation. While the Yb effect cannot be excluded from the process, the almost linear relationship between exsolved ions and Ce amount in the electrolyte points out that Ce is responsible for triggering the phenomenon.

To investigate possible cross-interface ion diffusion, we carried out time-of-flight secondary ion mass spectrometry (TOF-SIMS) at the cross-section of PCNC-AT/BZY that did not exhibit exsolution and PCNC-AT/BZCYYb1711 that displayed the highest population of exsolved particles (Fig. 4f and g). The bar on the right indicates the signal intensity with the intensity increasing as the color palette shifts to red. As expected, Pr is identified and distributed across the PCNC-AT positrode layer, while Ba and possibly Ce (mostly at the interface) were also identified at the outer monolayers of the positrode grains. Regarding Ce, HRTEM-EDX was used for identifying the elemental distribution and possible deeper penetration of migrating species from the electrolyte to the positrode. Notable Ce amounts are most likely present at the PCNC-AT electrode while the intensity for Ba was negligible (Fig. S18).

Ba volatilization from Ba-containing electrolytes is a known phenomenon during the sintering process at high temperatures. While the amount of evaporated Ba has been reported to be higher in Ce-containing electrolytes.[43,44] For instance, Fig. 4f shows that high Ba concentration is present even in the Ce-free BZY case. This result underpins that Ba cannot be considered as the sole cause of exsolution since no nanoparticles were observed in the BZY case, despite Ba evaporation. Moreover, the ionic radii of Ba^{2+} at the expected coordination for A-site doping is significantly higher than Pr^{3+}, rendering a possible substitution of Pr^{3+} less likely. Nevertheless, Ba evaporation from the A-site of BZCYYb may release free CeO_2 that can interact with the positrode at the interface or even substituting Pr due to the closer ionic radii and ultimately triggering the Pr_6O_{11} exsolution.[45,46]

Exsolution from perovskites is a process driven by lattice strain, and its activation energy barrier decreases in the presence of bulk and surface defects.[42,47,48] Here, a partial Pr^{3+} substitution with smaller size Ce^{4+} close to the interface could lead to lattice shrinkage and local compressive strain, thereby inducing Pr^{3+} migration outward to relieve the internal stress during sintering at elevated temperatures. Moreover, the enhanced concentration of oxygen vacancies after Ca doping and/or acid treatment in combination with Ce^{4+} migration would facilitate PrO_x species precipitation. Our hypothesis is that the Pr exsolution process is initiated by the Ce^{4+} incorporation in the positrode lattice, thus triggering Pr migration to relieve local stress (Fig. 4h). Following this step, migration of Pr^{3+} ions continues, resulting in growth of particles at surface defects.

Electrocatalytic performance for H_2O electrolysis

To carry out the electrocatalytic studies, BZCYYb1711 was selected as the electrolyte for its known advantages of performance in combination with the highest exsolution rates from positrodes among the examined substrates. The adhesion of the positrode on BZCYYb1711 without employing extremely high temperatures was achieved by etching the electrolyte surface with nitric acid to increase roughness by selectively removing excess BaO.[49–52] The etching process was optimized by investigating different parameters, including nitric acid concentration and etching duration with the ultimate target being the highest roughness without creating gaps at the grain boundaries or undesired secondary phases (Fig. S19). Our optimization showed that 1% nitric acid for 30 s displayed the optimum results for rejuvenating the electrolyte–electrode interface as revealed by the impressive drop in ohmic resistance compared to the unetched electrolyte (Fig. S20).

Following the etching process, the positrodes were screen-printed on the BZCYYb1711/Ni-BZCYYb1711 half-cells and the cell was sintered at 1000 °C for 2 h (Fig. 5a and Fig. S21a). Electrochemical impedance spectroscopy with the corresponding distribution of relaxation times (DRT) and the linear scanning voltammograms at temperatures between 400 and 650 °C are displayed in Fig. 5b–g. The data were collected by supplying pure H_2 at the Ni-BZCYYb1711 negatrode and 20% steam diluted in air at the positrode inlet. The synergy between the exsolved nanostructures on a TIEC and Ca doping resulted in considerably low polarization resistances (R_p) of 0.11 and 0.20 Ω cm^2 at 500 °C and 450 °C under the applied bias of 1.3 V, respectively, 2.7–4.4 fold lower than that of the other three types of air electrodes (PNC: 0.44 and 0.98 Ω cm^2, PNC-AT: 0.40 and 0.98 Ω cm^2, PCNC-AT: 0.30 and 0.78 0.98 Ω cm^2) (Fig. 5b and Fig. S22).

Distribution of relaxation times (DRT) of the four cells at 500 °C highlights the superior electrochemical kinetics of PCNC among the four electrodes, as shown in Fig. 5c. The positrodes mainly presented three distinct frequency regions: high-frequency (HF), intermediate-frequency (IF), and low-frequency (LF) regions that are associated with charge transfer processes, oxygen surface exchange kinetics and gas diffusion processes, respectively.[53,54] The peak intensities follow the order of PNC > PNC-AT > PCNC > PCNC-AT across the entire

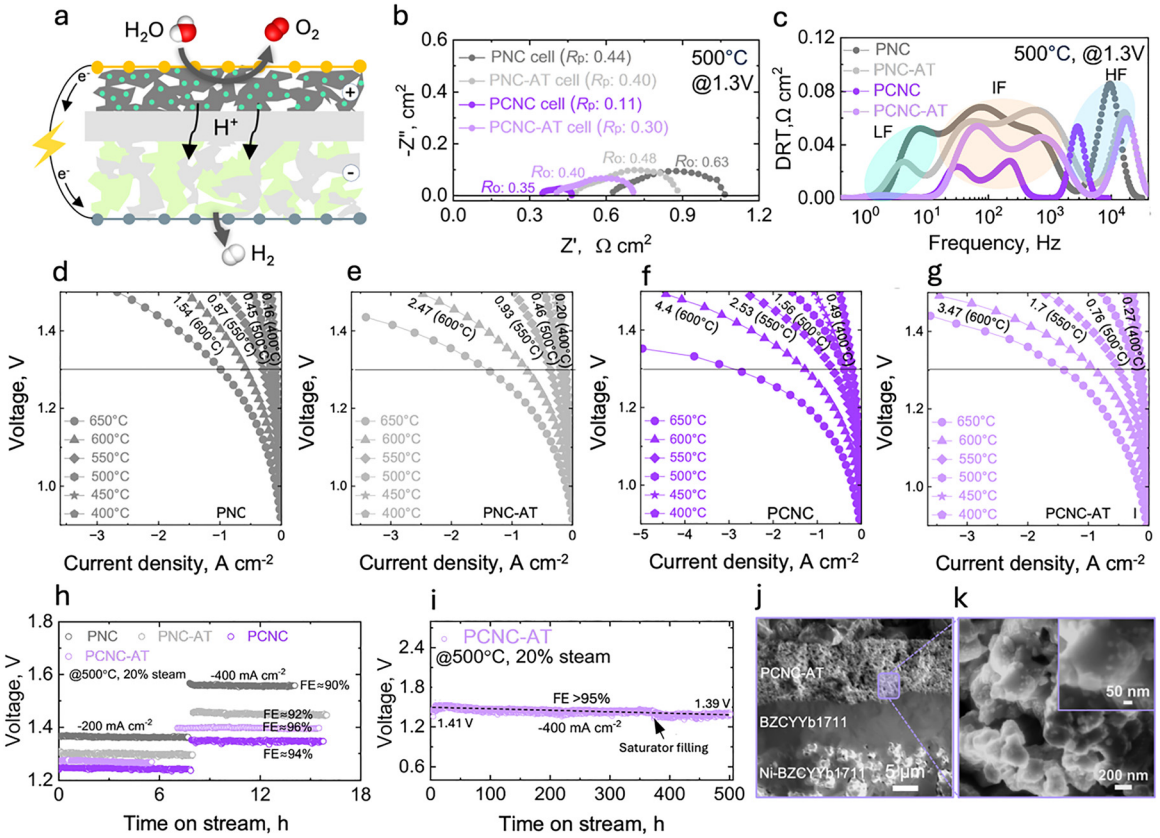


Fig. 5 Electrocatalytic performance for steam electrolysis. (a) Schematic of PCECs in electrolysis mode and the corresponding feed at the positrode and negatrode side. (b) Nyquist plots for the four samples in 20% H_2O/air under 1.3 V of applied bias (close to thermoneutral) at 500 °C and (c) the corresponding DRT analysis. *I–V* curves for (d) PNC, (e) PNC-AT, (f) PCNC, and (g) PCNC-AT positrodes in 20% H_2O/air at 400–650 °C. (h) Short-term stability of the PNC, PNC-AT, PCNC and PCNC-AT cells at applied currents of −0.2 A cm^{-2} and −0.4 A cm^{-2}. (i) Long-term stability test of the PCNC-AT cell at −0.4 A cm^{-2} for 500 h at 500 °C. (j) and (k) Cross-section SEM of the PCNC-AT-electrolyte interface following the durability test, revealing adequate positrode adhesion and nanoparticle aging.

frequency ranges, implying faster charge transfer, oxygen surface exchange and gas diffusion on the PCNC electrode. Benefiting from the enhanced oxygen exchange rates, higher concentration of oxygen vacancies and water uptake properties due to Ca doping (see also DFT section below), the PCNC electrode delivered current densities of 2.91, 1.31, 0.67, and 0.40 A cm^{-2} under an applied bias of 1.3 V at 650, 600, 550, and 450 °C, respectively, corresponding to 2–3-fold enhancement over pristine PNC.

Benchmarking against recent PCEC literature can be misleading as small differences in the testing parameters (*e.g.*, positrode area, flowrates, impurities, current collection, *etc.*) may be critical when investigating materials in different lab environments with insufficient control over humidity or impurities. Nonetheless, Fig. S23 and Table S6 compare the performance of PCNC and PCNC-AT electrodes at 1.3 V, revealing that the current densities achieved are higher than those of most of the state-of-the art electrodes reported, further corroborating to the effectiveness of our electrode functionalization strategy.

Following acid treatment, the PNC performance was also improved as for example at 650 °C where the current density increased to 1.36 from 0.99 A cm^{-2} at the thermoneutral voltage. Notably, the PCNC-AT electrode, while it displayed the largest amount of exsolution, exhibited lower current densities for steam electrolysis than PCNC, 1.41, 0.97 and 0.16 A cm^{-2} at 650, 550 and 450 °C, respectively. This is most likely attributed to a significant removal of CaO following acid treatment which decreases the water uptake capability as will be discussed in the DFT modeling section below.

To distinguish the contributions of Ca doping and acid treatment, pure $Pr_{0.97}Ca_{0.03}Ni_{0.5}Co_{0.5}O_{3-\delta}$ (denoted as PCNC97) was synthesized by the sol–gel method and characterized by XRD (Fig. S24). 3% Ca doping was selected as it corresponds to the amount of Ca in PCNC-AT due to the acid treatment according to the ICP-OES analysis (Fig. S2). The collected *I–V* curves for steam electrolysis performance of the PCNC97-based PCEC in 20% H_2O–air (Fig. S25) reveal that acid treatment in PCNC-AT is highly beneficial for the cell performance at all temperatures explored. Nevertheless, as the temperature is lowered to <500 °C, the beneficial effect of acid treatment is diminished, and the observed performance of PCNC97 is almost the same as that of PCNC-AT.

Although current density at the lowest possible overpotential is important for positrodes, it cannot be the sole performance indicator. Cell reactors should also be evaluated for steady-state

 This journal is © The Royal Society of Chemistry 2026

hydrogen production to ultimately define the faradaic and thus energy efficiency of the PCEC. For this investigation, the four cells were tested at 500 °C in the presence of 20% steam in air and the cell products were monitored using an online gas chromatograph and an electronic flowmeter to calculate faradaic efficiency (FE). By applying −0.2 and −0.4 A cm^{-2} for 8 h each, there was no substantial voltage increase, while PCNC and PCNC-AT required significantly less cell voltage for achieving the same current densities (Fig. 5h, SEM after testing in Fig. S26). The faradaic efficiencies at these current densities were calculated to be >90% in all cases (PCNC-AT reached 96%), confirming that our nanoengineered positrodes were indeed electrolyzing steam.

For long-term durability, the PCNC-AT sample that exhibited the highest faradaic efficiency was selected by applying a constant current of −0.4 A cm^{-2} and monitoring the voltage and the produced hydrogen for an extensive period of >500 h (Fig. 5i). The cell displayed outstanding stability during the long-term test, with even a slight decrease of cell voltage from 1.41 V to 1.39 V in 500 h, whereas a >95% FE was calculated at different points throughout the study. Post-mortem analysis was carried out on the cell using XRD and SEM (Fig. S27 and Fig. 5j, k). Following the durability test some minor delamination of the Ag current collector as well as some $BaCO_3$ (originating from BaO) secondary phases on the ceramic electrolyte were identified that could affect performance. Regarding the PCNC-AT positrode and the positrode-ceramic electrolyte interface, the cross-sectional SEM analysis (Fig. 5j and k) revealed no visible cracks or delamination of the positrode. Meanwhile, numerous exsolved Pr_6O_{11} nanoparticles could still be

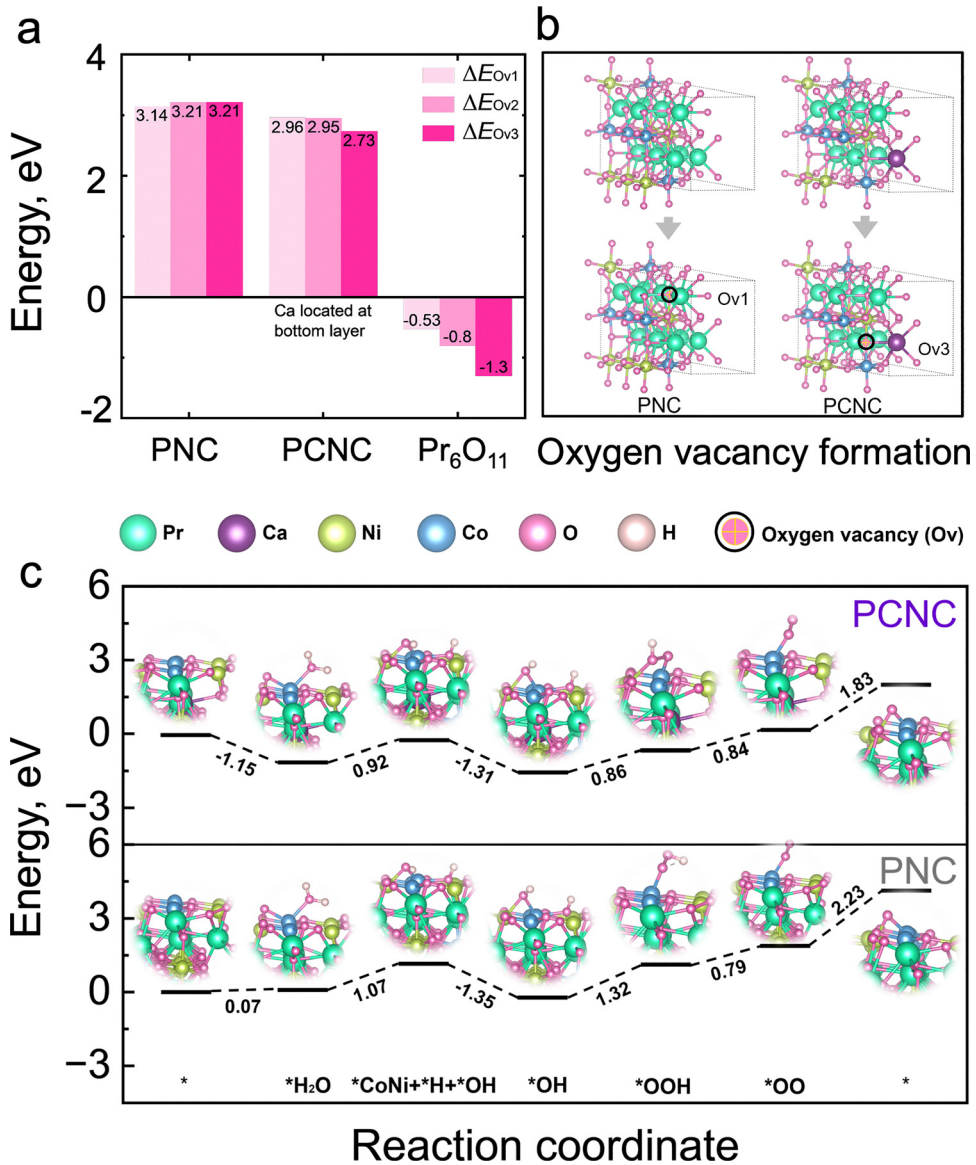


Fig. 6 DFT calculations of the steam splitting pathway. (a) The calculated optimal ΔE_{Ov} for PNC, PCNC, and Pr_6O_{11}. (b) Lattice structure with the most stable oxygen vacancy site in PNC and PCNC. (c) Energy profiles for the elemental steps of the OER on the surface of PNC and PCNC.

observed, exhibiting a modest increase in particle size compared to the fresh PCNC-AT sample (Fig. 5k).

To elucidate further the origins of the performance enhancement due to praseodymium oxide nanoparticles and Ca doping, we employed DFT calculations for the critical steps in H_2O electrolysis, starting with the oxygen vacancy formation energy (ΔE_{Ov}). We have considered two possible positions (bottom/top, middle) of Ca doping sites within the crystal structure model and all different configurations with oxygen vacancy to calculate the ΔE_{Ov} values (Fig. 6a–c and Fig. S28–S33). The ΔE_{Ov} related to Ov1, Ov2, and Ov3 exhibit a decreasing order of PNC > PCNC > Pr_6O_{11}. For example, the lowest ΔE_{Ov} in PNC is 3.14 eV, which is 0.41 eV higher than that of PCNC (2.73 eV) and 4.4 eV higher than that of Pr_6O_{11} (−1.3 eV). Such results confirm that PCNC and Pr_6O_{11} possess higher concentration of oxygen vacancies compared to PNC, indicating that Ca doping and Pr_6O_{11} exsolution effectively enhance the hydration capability and oxygen kinetics in agreement with the XPS, EPR and O_2-TPD experimental findings (Fig. 2 and Fig. S15).

We also investigated the adsorption energy of H_2O and the migration energetics of protons in PNC and PCNC with the most stable oxygen vacancy site. As shown in Fig. 6, the adsorption of H_2O exhibits an energy increase of 0.07 eV in PNC, yet an obvious energy decrease of −1.15 eV in PCNC. The adsorption of H_2O on Pr_6O_{11} particles has a large energy decrease of −2.26 eV, indicating that higher populations of Pr_6O_{11} nanoparticles in PCNC facilitate commensurate interactions with the reaction intermediates (Fig. S33). The proton of H_2O hops to the nearby O atom and it should cross/bind to a Ni atom, which requires 0.92 eV in PCNC, and 1.07 eV in PNC. The subsequent hydrogen transfer from the Ni site to the nearby O atom is an energy decrease, with similar values for PCNC and PNC (−1.31 *vs.* −1.35 eV, respectively). Subsequent steps are energetically unfavorable on both surfaces, with molecular O_2 formation incurring a large energy increase, amounting to 1.83 eV for PCNC and 2.23 eV for PNC. Overall, the proton migration energy in PCNC is 0.15 eV lower than that of PNC, while the energy required for the uphill (energy-climbing) steps is reduced by 0.81 eV when employing PCNC over PNC. The above findings in combination with our extensive experimental studies prove the beneficial role of Ca and higher populations of Pr_6O_{11} nanoparticles in boosting the performance of PCNC samples for steam splitting.

Conclusions

PCECs display the unique feature of being capable of operating at an intermediate temperature range that may unlock direct electrification of chemical processes when suitable electrodes are used. Our study introduced for the first time the choice of the ceramic electrolyte as a critical parameter for defining the high electrocatalytic activity of the positrode itself. We employed a simple perovskite structured PNC with triple conducting (O^{2-}, H^+, e^-) properties on a ceramic electrolyte where possibly free Ce ions from the electrolyte after Ba evaporation interact at the interface of the positrode and electrolyte, resulting in the decoration of the PNC-based electrode surface with exsolved Pr_6O_{11} nanoparticles (10–13 nm, 250–950 μm^{-2}). Additionally, Ca doping at the A-site was utilised to boost key properties for the OER such as the concentration of oxygen vacancies, water uptake and proton migration as supported by experimental characterization techniques and DFT modeling. The synergy between Pr_6O_{11} exsolution and Ca doping allowed 2–3 times higher current densities and hydrogen production than the pristine PNC by concurrently achieving >95% faradaic efficiency while exhibiting excellent stability for several weeks of continuous operation (500 h). Our results demonstrate for the first time the critical role of cross-interface ion diffusion in creating multifunctional heterostructures that may assist PCECs to achieve commercially viable performance.

Author contributions

Conceptualization: V. K.; experimental methodology: N. L., J. I. and V. K.; experimental data and data analysis: N. L., L. Z., W. H., P. H., and H. B.; DFT modeling: S. Z.; visualization: N. L. and V. K.; funding acquisition: V. K.; supervision: V. B., A. B. and V. K.; writing first draft: N. L. and V. K.; review and editing: all authors.

Conflicts of interest

There are no conflicts to declare.

Data availability

The authors confirm that the data supporting the findings in this study are available within the article and included as part of the supplementary information (SI). Supplementary information is available. See DOI: https://doi.org/10.1039/d6ee03199d.

Acknowledgements

This research has received funding from the European Union under grant agreement no 101099717 (ECOLEFINS project) and UK Research and Innovation (UKRI) under the UK governments Horizon Europe funding Guarantee (10079292). Views and opinions expressed are, however, those of the authors only and do not necessarily reflect those of the European Union or European Innovation Council and SMEs Executive Agency (EISMEA) or UK Research and Innovation granting authorities. Neither the European Union nor the granting authorities can be held responsible for them. N. Li would like to acknowledge the funding from China Scholarship Council (CSC) under Grant Number 202006060035.

References

1 H. Tian, *et al.*, Conformally coated scaffold design using water-tolerant $Pr_{1.8}Ba_{0.2}NiO_{4.1}$ for protonic ceramic

 This journal is © The Royal Society of Chemistry 2026

electrochemical cells with 5000 h electrolysis stability, *Nat. Energy*, 2025, **10**, 890–903.
2 R. O'Hayre, Full steam ahead: protonic ceramic cells, *Nat. Energy*, 2025, **10**, 800–801.
3 P. Babilo and S. M. Haile, Enhanced sintering of yttrium-doped barium zirconate by addition of ZnO, *J. Am. Ceram. Soc.*, 2005, **88**, 2362–2368.
4 D. Pergolesi, *et al.*, High proton conduction in grain-boundary-free yttrium-doped barium zirconate films grown by pulsed laser deposition, *Nat. Mater.*, 2010, **9**, 846–852.
5 M. Li, F. Liu and D. Ding, Critical insights into the steam electrolysis electrode in protonic ceramic cells for hydrogen production, *Nat. Catal.*, 2025, **8**, 293–300.
6 N. Li, A. Zarkadoulas and V. Kyriakou, Opportunities and challenges for direct electrification of chemical processes with protonic ceramic membrane reactors, *Prog. Energy*, 2024, **6**, 043007.
7 V. Kyriakou, I. Garagounis, A. Vourros, E. Vasileiou and M. Stoukides, An electrochemical haber-bosch process, *Joule*, 2020, **4**, 142–158.
8 I. Quina, *et al.*, Direct electrocatalytic CO_2 reduction in a pressurized tubular protonic membrane reactor, *Chem. Catal.*, 2023, **3**(10), 100766.
9 D. Poetzsch, R. Merkle and J. Maier, Proton uptake in the H + -SOFC cathode material $Ba_{0.5}Sr_{0.5}Fe_{0.8}Zn_{0.2}O_{3-\delta}$: transition from hydration to hydrogenation with increasing oxygen partial pressure, *Faraday Discussions*, 2015, **182**, 129–143.
10 M. Papac, V. Stevanović, A. Zakutayev and R. O'Hayre, Triple ionic–electronic conducting oxides for next-generation electrochemical devices, *Nat. Mater.*, 2021, **20**, 301–313.
11 K. Leonard, Y. Okuyama, M. E. Ivanova, W. A. Meulenberg and H. Matsumoto, Tailored and improved protonic conductivity through Ba $(Z_xCe_{10-x})_{0.08}Y_{0.2}O_{3-\delta}$ ceramics perovskites type oxides for electrochemical devices, *ChemElectroChem*, 2022, **9**, e202101663.
12 C. Herradon, *et al.*, Proton-conducting ceramics for water electrolysis and hydrogen production at elevated pressure, *Front. Energy Res.*, 2022, **10**, 1020960.
13 C. Duan, *et al.*, Highly efficient reversible protonic ceramic electrochemical cells for power generation and fuel production, *Nat. Energy*, 2019, **4**, 230–240.
14 H. Ding, *et al.*, Self-sustainable protonic ceramic electrochemical cells using a triple conducting electrode for hydrogen and power production, *Nat. Commun.*, 2020, **11**, 1907.
15 E. Vøllestad, *et al.*, Mixed proton and electron conducting double perovskite anodes for stable and efficient tubular proton ceramic electrolysers, *Nat. Mater.*, 2019, **18**, 752–759.
16 S. Choi, T. C. Davenport and S. M. Haile, Protonic ceramic electrochemical cells for hydrogen production and electricity generation: exceptional reversibility, stability, and demonstrated faradaic efficiency, *Energy Environ. Sci.*, 2019, **12**, 206–215.
17 M. Saqib, *et al.*, Transition from perovskite to misfit-layered structure materials: a highly oxygen deficient and stable oxygen electrode catalyst, *Energy Environ. Sci.*, 2021, **14**, 2472–2484.
18 F. Liu, *et al.*, Lowering the operating temperature of protonic ceramic electrochemical cells to <450 °C, *Nat. Energy*, 2023, **8**, 1145–1157.
19 F. He, *et al.*, An efficient high-entropy perovskite-type air electrode for reversible oxygen reduction and water splitting in protonic ceramic cells, *Adv. Mater.*, 2023, **35**, 2209469.
20 Y. Zhou, *et al.*, An active and robust air electrode for reversible protonic ceramic electrochemical cells, *ACS Energy Lett.*, 2021, **6**, 1511–1520.
21 K. Park, *et al.*, Water-mediated exsolution of nanoparticles in alkali metal-doped perovskite structured triple-conducting oxygen electrocatalysts for reversible cells, *Energy Environ. Sci.*, 2024, **17**, 1175–1188.
22 J. Yun, *et al.*, Highly active air electrode with enhanced proton conduction via isovalent doping in a layered perovskite for reversible protonic ceramic cells, *Adv. Funct. Mater.*, 2025, **35**, 2508758.
23 S. Zheng, *et al.*, Hybridizing electrode interface structures in protonic ceramic cells for durable, reversible hydrogen and power generation, *Adv. Mater.*, 2025, **37**, 2503649.
24 J. Xia, *et al.*, Self-configured composites of ruddlesden-popper perovskite and Pr6O11 as efficient and durable air electrodes for reversible protonic ceramic electrochemical cells, *Adv. Energy Mater.*, 2023, **13**, 2302964.
25 J. Xia, *et al.*, Regulation of Ni/Co Ratio and Gas Transport in High-Order Ruddlesden–Popper Perovskite Air Electrodes for Protonic Ceramic Electrochemical Cells, *Adv. Funct. Mater.*, 2024, **34**, 2403493.
26 V. Kyriakou, *et al.*, Plasma driven exsolution for nanoscale functionalization of perovskite oxides, *Small Methods*, 2021, **5**, 2100868.
27 J. T. Irvine, *et al.*, Evolution of the electrochemical interface in high-temperature fuel cells and electrolysers, *Nat. Energy*, 2016, **1**, 15014.
28 S. Wang, J. Zhu, S. A. Carabineiro, P. Xiao and Y. Zhu, Selective etching of in-situ formed La_2O_3 particles to prepare porous $LaCoO_3$ perovskite for catalytic combustion of ethyl acetate, *Appl. Catal., A*, 2022, **635**, 118554.
29 Y. Tang, *et al.*, Fabrication of oxygen-vacancy abundant NiMn-layered double hydroxides for ultrahigh capacity supercapacitors, *Adv. Funct. Mater.*, 2020, **30**, 1908223.
30 Y.-L. Lee, J. Kleis, J. Rossmeisl, Y. Shao-Horn and D. Morgan, Prediction of solid oxide fuel cell cathode activity with first-principles descriptors, *Energy Environ. Sci.*, 2011, **4**, 3966–3970.
31 Y. Chen, *et al.*, A robust and active hybrid catalyst for facile oxygen reduction in solid oxide fuel cells, *Energy Environ. Sci.*, 2017, **10**, 964–971.
32 X. Zhang, *et al.*, Novel high-entropy air electrodes enhancing electrochemical performances of reversible protonic ceramic cells, *Adv. Funct. Mater.*, 2025, **35**, 2421083.
33 Z. Liu, *et al.*, Steam-induced cation exchange in oxygen electrodes for superior protonic solid oxide cells, *Joule*, 2026, **10**(10), 102491.
34 W. Tang, *et al.*, An unbalanced battle in excellence: revealing effect of Ni/Co occupancy on water splitting

and oxygen reduction reactions in triple-conducting oxides for protonic ceramic electrochemical cells, *Small*, 2022, **18**, 2201953.
35 S. Zhai, *et al.*, A combined ionic Lewis acid descriptor and machine-learning approach to prediction of efficient oxygen reduction electrodes for ceramic fuel cells, *Nat. Energy*, 2022, **7**, 866–875.
36 M. Joos, X. Kang, R. Merkle and J. Maier, Water uptake of solids and its impact on ion transport, *Nat. Mater.*, 2025, **24**, 821–834.
37 J. Wu, *et al.*, A new nanocomposite electrode developed from environmental atmosphere triggered reconstruction for efficient reversible protonic ceramic cells, *Adv. Energy Mater.*, 2025, **15**, 2404118.
38 S. Dey, *et al.*, Bi-Functional Oxygen Electrocatalysts for Reversible Solid Oxide Cells: The Influence of A-Site Non-stoichiometry on the System $(La\ or\ Ba)_{0.6-x}Sr_{0.4}Co_{0.8}Fe_{0.2}O_{3-\delta}$, *ACS Appl. Energy Mater.*, 2025, **8**, 7433–7449.
39 C. Riedl, *et al.*, Surface decorations on mixed ionic and electronic conductors: effects on surface potential, defects, and the oxygen exchange kinetics, *ACS Appl. Mater. Interfaces*, 2023, **15**, 26787–26798.
40 C. Nicollet, *et al.*, Acidity of surface-infiltrated binary oxides as a sensitive descriptor of oxygen exchange kinetics in mixed conducting oxides, *Nat. Catal.*, 2020, **3**, 913–920.
41 D. Han, X. Liu, T. S. Bjørheim and T. Uda, Yttrium-doped barium zirconate-cerate solid solution as proton conducting electrolyte: why higher cerium concentration leads to better performance for fuel cells and electrolysis cells, *Adv. Energy Mater.*, 2021, **11**, 2003149.
42 K. Kousi, D. Neagu, L. Bekris, E. I. Papaioannou and I. S. Metcalfe, Endogenous nanoparticles strain perovskite host lattice providing oxygen capacity and driving oxygen exchange and CH4 conversion to syngas, *Angew. Chem., Int. Ed.*, 2020, **59**, 2510–2519.
43 Y.-D. Kim, *et al.*, Tuning barium release from sacrificial powders to optimize sintering and enhance the performance of reversible large-scale tubular protonic ceramic electrochemical cells, *J. Power Sources*, 2025, **625**, 235700.
44 D. Han, *et al.*, Strategy to improve phase compatibility between proton conductive $BaZr_{0.8}Y_{0.2}O_{3-\delta}$ and nickel oxide, *RSC Advances*, 2016, **6**(23), 19288–19297.
45 Y. Chen, *et al.*, An in situ formed, dual-phase cathode with a highly active catalyst coating for protonic ceramic fuel cells, *Adv. Funct. Mater.*, 2018, **28**, 1704907.
46 J. Hou, *et al.*, A novel in situ diffusion strategy to fabricate high performance cathodes for low temperature proton-conducting solid oxide fuel cells, *J. Mater. Chem. A*, 2018, **6**, 10411–10420.
47 J. Wang, *et al.*, Fast surface oxygen release kinetics accelerate nanoparticle exsolution in perovskite oxides, *J. Am. Chem. Soc.*, 2023, **145**, 1714–1727.
48 V. Kyriakou, *et al.*, Symmetrical exsolution of Rh nanoparticles in solid oxide cells for efficient syngas production from greenhouse gases, *ACS Catal.*, 2020, **10**, 1278–1288.
49 S. Choi, *et al.*, Exceptional power density and stability at intermediate temperatures in protonic ceramic fuel cells, *Nat. Energy*, 2018, **3**, 202–210.
50 M. Choi, in Electrochemical Society Meeting Abstracts 243. 271–271 (The Electrochemical Society, Inc.).
51 S. Haile, G. Staneff and K. Ryu, Non-stoichiometry, grain boundary transport and chemical stability of proton conducting perovskites, *J. Mater. Sci.*, 2001, **36**, 1149–1160.
52 W. Bian, *et al.*, Revitalizing interface in protonic ceramic cells by acid etch, *Nature*, 2022, **604**, 479–485.
53 M. Fei, *et al.*, The interlayer proton capture and transport mechanism in oxygen electrodes boosts proton ceramic electrolysis, *Energy Environ. Sci.*, 2026, **19**, 349–358.
54 Y. Tian, *et al.*, A high-entropy composite air electrode with dual-phase exsolution for efficient reversible proton ceramic cells, *Adv. Funct. Mater.*, 2026, **36**, e74663.

 This journal is © The Royal Society of Chemistry 2026